Degradation Study by Start-up/Shut-down Cycling of Superhydrophobic Electrosprayed Catalyst Layers Using a Localized Reference Electrode Technique.

Journal:	*ACS Applied Materials & Interfaces*
Manuscript ID	am-2016-15581c.R1
Manuscript Type:	Article
Date Submitted by the Author:	15-Feb-2017
Complete List of Authors:	Ferreira-Aparicio, Paloma; Centro de Investigaciones Energeticas Medioambientales y Tecnologicas Chaparro, Antonio; Centro de Investigaciones Energeticas Medioambientales y Tecnologicas Folgado, Maria; Centro de Investigaciones Energeticas Medioambientales y Tecnologicas Conde, Julio; Centro de Investigaciones Energeticas Medioambientales y Tecnologicas Brightman, Edward; National Physical Laboratory Hinds, Gareth; National Physical Laboratory

Degradation Study by Start-up/Shut-down Cycling of Superhydrophobic Electrosprayed Catalyst Layers Using a Localized Reference Electrode Technique.

Paloma Ferreira-Aparicio[1]‡, Antonio M. Chaparro[1‡], M. Antonia Folgado[1], Julio J. Conde[1], Edward Brightman[2‡], Gareth Hinds[2‡].*

[1] CIEMAT-Centro de Investigaciones Energéticas, Medioambientales y Tecnológicas. Avda. Complutense 40, E-28040. Madrid. Spain.

[2] National Physical Laboratory, Teddington, Middlesex, TW11 0LW, United Kingdom.

KEYWORDS: Electrosprayed films; superhydrophobic catalyst layer; Pt:C ratio; cathode localized potential; reference electrode array; startup/shut-down degradation.

ABSTRACT Degradation of a polymer electrolyte membrane fuel cell (PEMFC) with electrosprayed cathode catalyst layers is investigated during cyclic start-up and shut-down events. The study is carried out within a single cell incorporating an array of reference electrodes that enables measurement of cell current as a function of local cathode potential (localized polarization curves). Accelerated degradation of the cell by start-up/shut-down cycling gives rise to inhomogeneous performance loss, which is more severe close to the gas outlet and occurs predominantly during start-up. The degradation consists primarily of loss of cathode catalyst activity and increase in cell internal resistance, which is attributed to carbon corrosion and Pt aggregation in both anode and cathode. Cells with an electrosprayed cathode catalyst layer show lower degradation rates during the first 100 cycles, compared with a conventional gas diffusion electrode. This difference in behavior is attributed to the high hydrophobicity of the electrosprayed catalyst layer microstructure, which retards the kinetics of corrosion of the carbon support. In the long term, however, the degradation rate is dominated by the Pt:C ratio in the cathode catalyst layer.

INTRODUCTION

Polymer electrolyte membrane fuel cell (PEMFC) technology is a promising solution to power portable devices and as a zero-emission power source for automotive applications, but its widespread commercialization is still hindered by durability limitations. Lifetime targets of 40.000 h for stationary applications and 5.000 h for transport, which were established in the last Hydrogen and Fuel Cells Program Plan released by the US Department of Energy[1], are still to be overcome in a commercial system[2]. The performance decay of a fuel cell stack over time is primarily due to material degradation in the individual cell components, including the membrane, catalyst layer (CL), microporous layer (MPL), gas diffusion layer (GDL), bipolar plate (BP), and seals[3-9]. Determining the factors dominating the degradation rate in these systems is critical for enhancing their durability.

In many fuel cell applications, start-up and shut down (SU/SD) of the system has the most significant impact on cell durability due to transient changes in load and gas feed, which poses a severe limitation on the lifetime of the system. To analyze this important decay process, accelerated degradation tests are commonly carried out by repetitive SU/SD cycling, consisting of parallel changes in the gas feed of the anode and cell load. Carbon corrosion and Pt dissolution are the main factors leading to cell degradation during SU/SD transients. Comprehensive models have been developed to analyze corrosion processes[10-12] in order to understand performance losses and improve cell durability[13], including experimental studies with local resolution using segmented cells for better understanding of the corrosion at different distances from the gas inlet[14]. However, the effects of SU/SD on observed variations in electrocatalyst activity and kinetics, CL structure and porosity, and material wetting properties (i.e., hydrophilicity) are difficult to separate unambiguously.[15]

In a previous study[16] the response of electrosprayed catalyst layers (ECLs) in the cathode of a PEMFC was studied with spatial mapping of electrode potential using cell hardware incorporating an array of reference electrodes. The through-plate reference electrode design used allowed for the measurement of the localized potential without iR drop, enabling the acquisition of local cathode polarization curves as a function of cell current.[17] It was shown that the use of ECLs improves homogeneity of cell performance compared to standard commercial electrodes, which was attributed to their enhanced hydrophobic properties. The ECLs are characterized by a mesoporous morphology that provides superhydrophobic surfaces and high water transport capability. In addition, the ionomer and platinum catalyst show a better distribution and closer interaction within the electrosprayed films. [18]

In this paper, we investigate the durability of PEMFC cathode ECLs using an accelerated degradation test consisting of SU/SD cycling. The aim of this work is to determine the influence of the electrosprayed morphology on the degradation rate of the cell. Membrane electrode assemblies (MEAs) were prepared by direct electrospray deposition of the cathode CL on the membrane, using catalysts with variable Pt:C ratio. Performance losses due to SU/SD cycling were measured at different positions across the active area of the MEAs using the reference electrode array technique, and compared with those obtained for a cathode CL prepared by a conventional deposition method.

EXPERIMENTAL SECTION

MEA preparation and characterization

Cathode CLs were prepared by electrospray deposition of the catalyst and ionomer on Nafion NRE212 membrane, as described elsewhere[19]. In this study, three catalysts with different Pt:C ratios were used: Pt (60 wt%) on high surface area advanced carbon (HSAAC) support (HiSPEC™ 9100, Alfa Aesar GMBH), Pt (40 wt%) on Vulcan XC72 (HiSPEC™ 4000, Alfa Aesar GMBH) and Pt (20 wt%) on Vulcan XC72 carbon black (ETEK). According to the manufacturer specifications, the Pt (60 wt%)/HSAAC and the Pt (40 wt%)/Vulcan XC72 have minimum surface areas of 85 $m^2_{Pt}\cdot g^{-1}$ and 60 $m^2_{Pt}\cdot g^{-1}$, as measured by CO chemisorption, and average Pt particle sizes of 2.8 nm and 3.4 nm, respectively[20]. It must be noted that the HSAAC support has higher surface area than Vulcan XC72, which allows for a good Pt dispersion even with such high platinum content. The Pt (20 wt%)/Vulcan XC72 has a surface area of 104 $m^2_{Pt}\cdot g^{-1}$ (measured by CO chemisorption) and an average Pt particle size of 2.7 nm.[21] Catalyst inks for the deposition of cathode ECLs were prepared in isopropanol by adding the corresponding amounts of catalyst and ionomer (Nafion in 5 wt% solution, Aldrich). The Nafion concentration in the ink was calculated to achieve 15 wt% of ionomer in the CL.[22] The suspensions were ultrasonically stirred for 1 h before use. For electrospray deposition of the catalyst, a high dc voltage (9 kV) was applied between the electrospray needle and the substrate. During the deposition process, the catalyst ink was maintained in a beaker submerged in a thermostatic bath at 22 ^{o}C under ultrasonic stirring, at a low N_2 overpressure (0.1 bar_g) to force the ink to flow towards the needle through a silica capillary (150 μm diameter). The ink flow rate ejected through the needle during the electrospraying process was 0.5 $ml\cdot h^{-1}$. This corresponds to a deposited amount of catalyst layer of 6 $mg\cdot h^{-1}$. The deposition was carried out directly onto a 7 cm x 7 cm active area of the Nafion membrane (NRE212, Ion Power, 51 μm thickness) placed on an x-y stage, which was maintained at a distance of 4 cm from the needle. The morphology of the pristine MEAs was analyzed by scanning electron microscopy (Hitachi FE-SEM SU-6600) following compression at 20 bar_g between the flow field plates.[23]

Table 1. Characteristics of the catalyst layers in the MEAs evaluated. Pt loading in the anode and the cathode is maintained in all cases at 0.25 mg·cm^{-2}.

MEA	Anode	Cathode	Cathode CL characteristics				
			Pt:C ratio	Thickness[a] (μm)	d_{Pt} [c] (nm)	Porosity (%) ϕ_1[d]/ϕ_2[e]	Contact angle[f] (deg)
ES60	GDE30	ES60 (Pt(60wt%)/HSAAC on NRE212) + GDL	1.50	18±5[b]	2.8 [20]	98/98	168
ES40	GDE30	ES40 (Pt(40wt%)/V-XC72 on NRE212) + GDL	0.67	33±10 [b]	3.4 [20]	97/98	167
ES20	GDE30	ES20 (Pt(20wt%)/V-XC72 on NRE212) + GDL	0.25	46±10 [b]	2.7 [24]	92/97	157
GDE30	GDE30	GDE30 (Pt(30wt%))/V-XC72)	0.43	12±1	3.5 [26]	81/78	106

[a] Measurements taken from SEM cross-section images of pristine MEAs after compression with a clamping pressure of 20 bar$_g$ between the flow field plates (torque of 3 N m corresponding to a force of 1 kN per screw as determined with calibrated springs (UNCETA, XM20025152, 63.5 N/mm).[23]

[b] Due to the high porosity and complex internal structure of these layers this value is given as a rough estimation.

[c] As measured by analyzing the broadening of the X-ray diffraction line corresponding to the [2 0 0] plane of Pt crystallites at 2Θ = 67.5°.

[d] Values estimated from CL thickness as measured by SEM assuming a minimum porosity calculated from the bulk density of the components (Pt: 21.45 g·cm^{-3}; carbon support: 0.26 g·cm^{-3}; Nafion: 1.97 g cm^{-3}).

[e] Values estimated from pore volume as measured by Hg porosimetry in Ref 18: the value 12.0 cm^3·g$_C^{-1}$, which corresponds to an electrosprayed film of Pt(20wt%)/Vulcan XC72 and 15wt% ionomer content, has been applied to all the electrosprayed layers; the value 1.8 cm^3·g$_C^{-1}$, which corresponds to an airbrushed film of Pt(20wt%)/Vulcan XC72 and 30wt% ionomer content, has been applied to the GDE30 commercial electrode.

[f] Measurement taken after 400 min of contact of the water drop on the surface (initial drop volume: 6.0 ± 0.5 μl).

The surface hydrophobicity of the CLs was analyzed by means of water contact angle measurements. An optical tensiometer (Theta 200 Basic, Biolin Scientific) was used for the measurements. The static contact angle and the drop volume were measured as a function of time for all the CLs deposited on the Nafion 212R membrane. For the measurements, the opposite face was firmly fixed to a flat plate to avoid membrane deformation. The static contact angle was measured at ambient temperature (23ºC) and relative humidity (30-35%) as a function of time. The properties of the resulting cathode CLs are summarized in **Table 1**.

For single cell mounting, in all cases an identical commercial gas diffusion electrode (GDE) from BASF was used for the anode (Pemeas, ELAT GDE LT120EWALTSI, 0.25 $mg_{Pt}\cdot cm^{-2}$, Pt (30 wt%)/Vulcan XC72). For the electrosprayed cathodes, a commercial gas diffusion layer (GDL) with microporous layer (MPL) (BASF – ELAT GDL LT1200W) was used together with the ECLs deposited on Nafion NRE212. In addition, a control cell was prepared with two commercial GDEs for anode and cathode and a Nafion NRE212 membrane. In the following discussion the tested MEAs are referred to as ES60, ES40, ES20 (electrosprayed cathodes with 60, 40 and 20 wt% Pt respectively) and GDE30 (control cell).

Cell testing

The resulting MEAs were tested in a single cell PEMFC with an array of nine reference electrodes. The through-plate reference electrode configuration has been described previously in detail.[25] Therefore, only a brief description of the setup is given here. One end of a length of Nafion tubing acting as a salt bridge is inserted into a glass vessel containing 0.5 M H_2SO_4, into which is placed a Hydroflex hydrogen reference electrode (Gaskatel GmbH, Germany). The other end is inserted through a hole in the end-plates of the cell and sealed using an O-ring. This tube makes contact with the GDL, which is impregnated with Nafion at the point of contact using a micro-pipette to dispense 2 μL of a Nafion dispersion (equal parts of 10% Nafion dispersion in water (Sigma Aldrich, UK) and 2,2,3,3-tetrafluoro-1-propanol (Sigma Aldrich, UK)). This creates a small circular region of ionic conductivity through the GDL approximately 3 mm in diameter at each measurement location that can probe the cathode potential in the CL with minimal resistance. Using nine such reference electrodes allows mapping of the spatial distribution of cathode potential across the active area of the cell. The locations of the points of contact with respect to the serpentine flow-field are shown in **Fig. 1.**

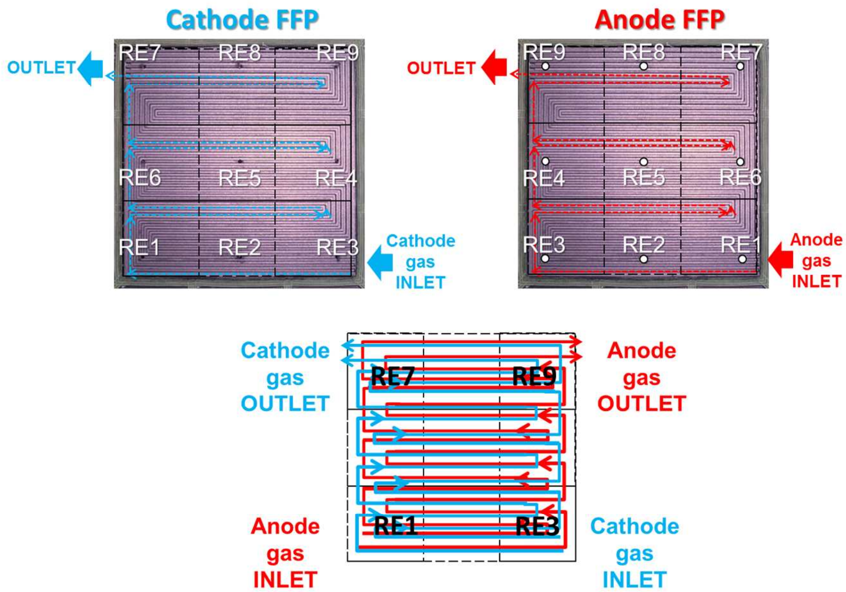

Figure 1. Location of the array of localized reference electrodes at the cathode with respect to the channels of the flow field plates (FFPs) of anode and cathode.

A six parallel channel serpentine flow-field made from resin-impregnated graphite with 1 mm x 1 mm channel cross-section was used on both anode and cathode in partial counter-flow mode (Fig. 1). Experiments were carried out using a Hydrogenics FCATSG50 test stand, with compression of the cell achieved using a pressurized gas/piston arrangement at a compression pressure of 7 bar_g. Prior to the measurements, the cells were pre-conditioned overnight at 80 ^oC

and 100% RH at a constant current of 0.5 A·cm^{-2} and 2 bar$_g$ backpressure on both anode and cathode.

Polarization curves were measured at 80 °C, 100% RH, and 1 bar$_g$ or 2 bar$_g$ backpressure on anode and cathode, using H_2/air at 2/2 stoichiometry. Local cathode potentials were measured versus the reversible hydrogen electrode (RHE) at the nine locations described above. Electrochemically active surface area (ECSA) of the cathode CL was measured by means of the hydrogen underpotential desorption charge method from a voltammetric curve obtained at 25 mV·s^{-1}, 35 °C, 100% RH, with H_2/N_2 at 30 sl·h^{-1}, in the potential range between 0.05 V and 0.80 V vs SHE.

Degradation of MEAs was achieved by applying successive start-up/shut-down (SU/SD) cycling to the cell at atmospheric pressure and 80 °C. During cycling, the cathode was fed with air at 30 sl·h^{-1}, while the anode gas and cell load was changed in five steps: 1) 12 sl·h^{-1} air (60 s); 2) 12 sl·h^{-1} H_2 (open circuit, 60 s); 3) load of 0.2 A cm^{-2} (10 s ramp, 40 s hold); 4) open circuit (10 s ramp); 5) 12 sl·h^{-1} air (60 s).

RESULTS AND DISCUSSION

Beginning of life (BoL) evaluation of the MEAs

The general characteristics of the MEAs with electrosprayed cathode CL and control cell are compiled in **Table 1**. Since all electrodes are prepared with the same Pt loading (0.25 mg$_{Pt}$·cm^{-2}), the resulting CLs differ in key parameters for cathode behavior, such as thickness, porosity, and Pt:C ratio. It must be noted that the ionomer content in electrospray deposited layers has been reduced to 15wt% as compared to the typical 30wt% optimum for conventionally prepared CLs such as the GDE30. As previously reported, the electrospray deposition procedure yields a particular ionomer distribution pattern that decreases the optimum ionomer content to 15wt% for a given ink composition.[22] Although the optimum amount could vary depending on the Pt loading of the catalyst, the 15wt% has been maintained for all the ECLs.

SEM images of the cross-sections of the pristine cathode ECLs deposited on the membrane and the GDE30 CL on the GDL microporous layer are included in **Fig. 2.** At first sight, the main difference between them is the microstructure of the CLs, being more compact for the commercial gas diffusion electrode GDE30 (**Fig. 2.d**) than for the ECLs (**Fig. 2.a-c**), whose high porosity is evident. Porosity values have been obtained by two different methods, as indicated in Table 1. Values calculated from the experimentally observed thickness of the CL (via SEM) compared with the nominal thickness of a fully dense film are indicated as ϕ_1. The nominal thickness was determined from the composition and density of the components (Pt, C and Nafion). The second method is based on the specific pore volume measured via Hg porosimetry in previous work[18], which for an electrosprayed layer is 12 $cm^3 \cdot g_C^{-1}$ and for a conventional layer (Pt(20wt%)/Vulcan XC72 catalyst with a 30wt% ionomer content and airbrush deposition) is 1.8 $cm^3 \cdot g_C^{-1}$. These values are indicated as ϕ_2 in Table 1. The results show good agreement between both approaches, with far higher porosity of the electrosprayed deposited layers compared with the conventional layer. The excess porosity of the electrosprayed layer is ascribed to meso and, mostly, macroporosity.[18] In addition, ECLs show increasing porosity in the order ES60>ES40>ES20, which reflects changes in the film deposition process, discussion of which is beyond the scope of this work. The relatively high thickness of ECLs and their lower ionomer content do not result in increased proton transport resistance, as previously reported for the ES20 sample; on the contrary, higher ionomer contents in electrosprayed samples yield lower performance.[18]

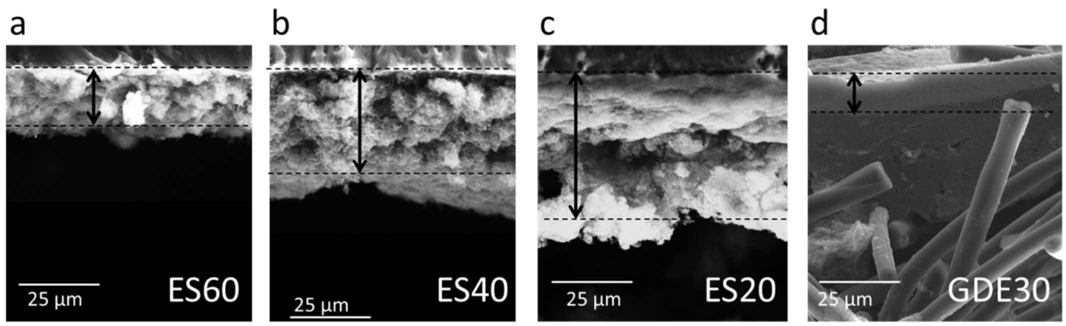

Figure 2. SEM micrographs of the cross-sections of pristine cathode electrodes: a) catalyst layer of the electrosprayed Pt(60wt%) on HSAAC on NRE212 (MEA ES60); b) catalyst layer of the electrosprayed Pt(40wt%) on Vulcan XC72 on NRE212 (MEA ES40); c) catalyst layer of the electrosprayed Pt(20wt%) on Vulcan XC72 on NRE212 (MEA ES20); d) standard gas diffusion electrode (ELAT-GDE- LT250EWALTSI) with Pt(30wt%) on Vulcan XC72 anode in ES60, ES40, ES20, and anode and cathode in GDE30.

Regarding the wettability of the CLs surfaces, the determined water contact angles (Table 1) reveal the superhydrophobic behavior of the electrospray-deposited layers (significantly greater than 150º) in contrast with the slightly hydrophobic GDE30 surface. At first sight, these differences could be ascribed to two main causes: on one hand, the lower ionomer content for optimized ECLs, and, on the other hand, the resulting porous microstructure of the electrosprayed surfaces. In order to elucidate the origin of the observed ECLs superhydrophobicity, new contact angle measurements were performed on three additional CLs, which were prepared for comparison with the ES20 layer containing 15wt% Nafion ionomer (ES20-15Naf). The first one was a new ECL prepared with 30 wt% Nafion ionomer content

(ES20-30Naf). Two other equivalent catalytic layers were prepared by a conventional method of aerography with the same catalytic inks containing 15 (AE20-15Naf) and 30 wt% Nafion ionomer (AE20-30Naf). Fig. 3a shows the water contact angle evolution of the catalyst layers prepared by aerography and by electrospray with identical inks containing 15 and 30 wt.% Nafion, respectively.

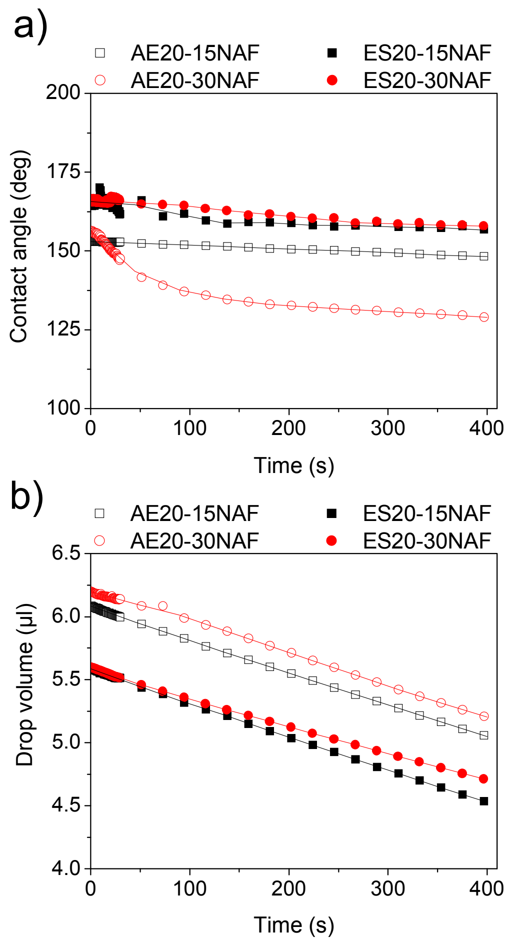

Figure 3. a) Water contact angles measured as a function of time on the surface of catalyst layers prepared by electrospray and aerography with 15 and 30 wt% ionomer. b) Evolution of the water drop volume with time. Symbols: aerography (open symbols); electrospray (solid symbols); 15wt% Nafion ionomer (squares), 30wt% Nafion ionomer (circles).

The Nafion ionomer content plays, as expected, a relevant role in the wettability of the catalyst layers prepared by a conventional spraying method such as the aerography. Although initially these layers show similar water contact angles (153º for AE20-15Naf and 155º for AE20-30Naf), the ionomer presence induces with time a higher interaction of the surface with water. The increase of the ionomer content from 15wt% to 30wt% reduces after several minutes the water contact angle by almost 20º to a value of 129º for the higher loaded sample. On the contrary, this effect is not shown for electrospray prepared layers. The initial water contact angles of the two ECLs clearly indicate that the electrospray deposition technique generates a different superhydrophobic microstructured surface, in which wettability does not depend on the Nafion ionomer content. They both maintain water contact angles close to 157º. The slight variation with time in the contact angle measurement can be ascribed to the decrease of the drop volume by evaporation (Fig. 3b).

The ECSA of each of the cathodes was measured in the cell at BoL. These results are included in **Table 2**. Values obtained can be considered similar and within the relative error expected for these kind of measurements[27], with the exception of ES60, which has a significantly higher ECSA value. It is observed that for the same average Pt crystallite size (d_{Pt}) the ECSA value increases with decreasing CL thickness: i.e. for catalysts with d_{Pt} between 2.7-2.8 nm, ECSA values are 37 $m^2 \cdot g^{-1}$ (ES20) and 49 $m^2 \cdot g^{-1}$ (ES60) depending on the CL thickness, and for catalysts with d_{Pt} 3.4-3.5 nm, ECSA is 34 $m^2 \cdot g^{-1}$ and 37 $m^2 \cdot g^{-1}$ for the thicker (ES40) and thinner layer (GDE30), respectively. This indicates a possible decrease of Pt utilization with increasing CL thickness, as observed by several groups. [28,29]

Table 2. ECSA, maximum power density (W_{max}), and parameters of the global polarization curves for MEAs ES60, ES40, ES20 and GDE30 at BoL and EoL (after SU/SD cycling). Values of b, $R_i(dc)$, and i_l were obtained by fitting the curves in Figs. 3.B and 3.D to equation 1.

MEA	ECSA $m^2 \cdot g_{Pt}^{-1}$	W_{max} $W \cdot cm^{-2}$	i_0 $10^{-7} A \cdot cm^{-2}$	b mV	$R_i(dc)$ $Ohm \cdot cm^2$	i_l $A \cdot cm^{-2}$
ES60 (BoL)	49	0.57	1.59	57	0.23	1.40
ES60 (EoL)	11	0.16	0.36	62	0.90	-
ES40 (BoL)	34	0.56	1.11	59	0.21	1.27
ES40 (EoL)	10	0.20	0.33	64	0.69	-
ES20 (BoL)	37	0.52	1.24	62	0.22	1.36
ES20 (EoL)	34	0.48	1.11	61	0.31	-
GDE30 (BoL)	37	0.53	1.20	58	0.21	1.21
GDE30(EoL)	11	0.32	0.36	55	0.50	-

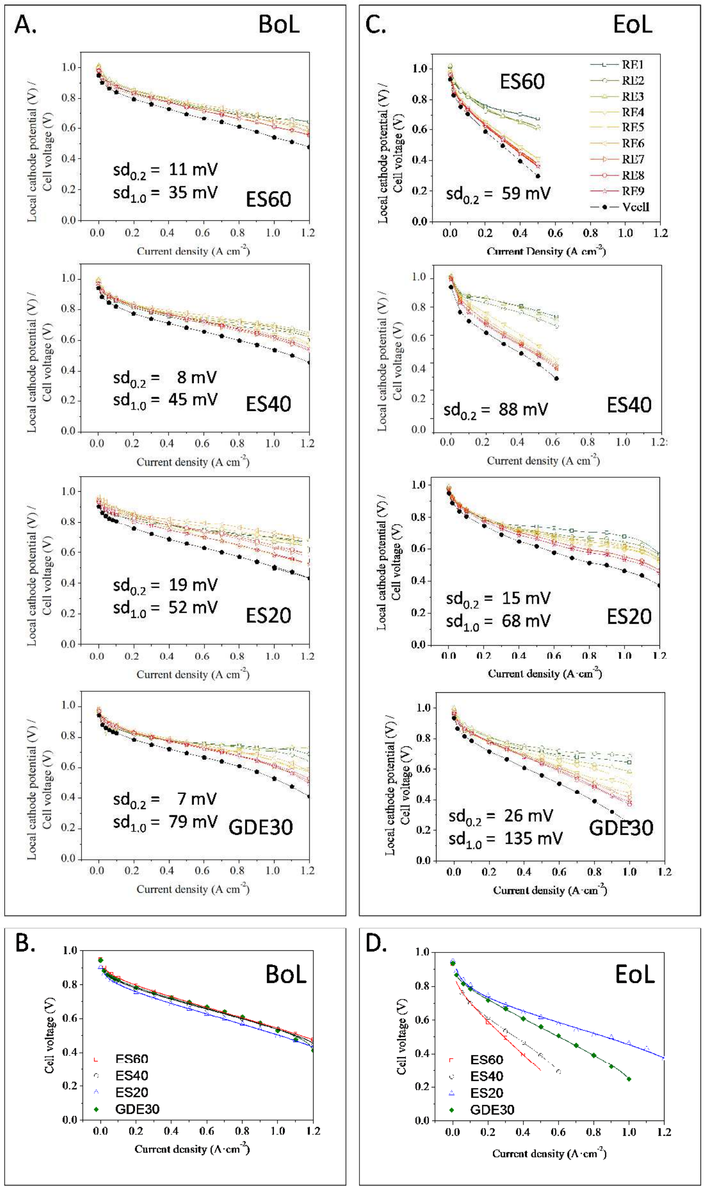

Figure 4. A) Cell voltage and local cathode potential as a function of current density at BoL for the four different MEAs. B) Comparison of polarization curves for the four MEAs at BoL. C) Cell voltage and local cathode potential as a function of current density at EoL (after 300 SU/SD cycles). D) Comparison of polarization curves for the four MEAs at EoL. Standard deviations of potential values at 0.2A·cm^{-2} ($sd_{0.2}$) and 1.0 A·cm^{-2} ($sd_{1.0}$) are indicated in A and C for each MEA.

The cell voltage and local potential at BoL are presented in **Fig. 4.A** as a function of the cell current density. A variable dispersion of local potential values is observed for the different cells. The degree of dispersion has been quantified at 0.2 $A\cdot cm^{-2}$ and 1.0 $A\cdot cm^{-2}$ by means of the standard deviation, $sd_{0.2}$ and $sd_{1.0}$, respectively, with calculated values included in each plot. At low current densities, the local cathode potential is less homogeneous for ECLs, characterized by $11 < sd_{0.2} < 19$ mV, (**Fig. 4.A**). The control MEA is characterized by more homogeneous dispersion ($sd_{0.2} = 7$ mV). At high current densities, the dispersion of the local cathode potential increases for all the MEAs tested, but it is now more pronounced for the control MEA ($sd_{0.2} = 79$ mV) than for ECLs, where dispersion decreases in the order ES20 > ES40 > ES60. The curves reveal a local performance decrease from inlet to outlet of the cathode flow stream, i.e. local cathode potential decreases from the positions of the reference electrodes RE1/RE3 at the anode/cathode inlet to RE9/RE7 at the anode/cathode outlet (cf. **Fig. 1**). Such inlet-to-outlet decrease in cell voltage reflects predominantly the effect of mass transport limitation at the cathode, which is higher for the control MEA (GDE30) than for electrosprayed MEAs. The control MEA shows more severe mass transport limitations, both qualitatively as shown by the increasing gradient of the polarization curve at high current density, and quantitatively measured by impedance spectroscopy as shown in a previous study[16]. The more homogeneous response in MEAs with cathode ECLs was attributed in a prior study to the superhydrophobic character of electrosprayed films.[16] For better comparison of the different MEAs, the global polarization curves obtained at BoL are compiled in **Fig. 4.B**.

Table 2 summarizes performance data of the MEAs, including ECSA, maximum power density, and parameters of the global polarization curves obtained by fitting to the standard macroscopic model expressed by equation 1:

$$V = E - b \cdot \log\left(\frac{i}{i_0}\right) - i \cdot R_i(dc) - b \cdot \log\left(\frac{i_l}{i_l - i}\right) \quad (1)$$

where V is the cell voltage, E the thermodynamic potential (E=1.195V, for H_2 and air at t=80°C, p=3 bar$_a$, and 100% RH), b the Tafel slope, i the current density, i_0 the exchange current density, $R_i(dc)$ the dc internal resistance, and i_l the limiting current density. The i_0 values referred to the electrode geometrical area were calculated from the catalyst loading (L_{Pt}), the exchange current density of a pure Pt surface ($i_{0,Pt}$), and the experimentally obtained ECSA also reported in Table 2 ($i_0 = i_{0,Pt} \cdot \text{ECSA} \cdot L_{Pt}$, taking L_{Pt}=0.25 mg·cm^{-2}, and $i_{0,Pt}$ =1.3·10^{-9} A·cm$^{-2}_{Pt}$)[30]. The transport limiting term was only applied for those curves with a well-defined limiting region.

Accelerated degradation tests

The cells were subjected to a cyclic degradation process that mimics repetitive SU/SD events in a stack, consisting of changes in the cell current load and in the gas fed into the anode, as detailed in the experimental section. The evolution of the local cathode potential at the different RE positions was registered during the cycles. **Fig. 5** illustrates the local transient response of the cathode potential for the GDE30 MEA during the first SU and SD events. Initially, before injecting hydrogen in the anode during SU, a spread of local cathode potentials is observed at inlet segments (RE1,2,3) **(Fig. 5a)**, which occurs again at the end, after injecting air into the anode during SD **(Fig. 5b)**. This behavior must be ascribed to the use of a dry supply of air alternating with a humid H_2 stream (80% RH) for cell operation. Once humid H_2 enters the cell, a potential transient is observed, following a bimodal or a positive spike of variable intensity depending on cathode location. This trend is consistent with that observed in segmented cells, and has been explained by the reverse current mechanism model first proposed by Reiser *et al.* [12]. According to this model, when hydrogen is introduced into the air-filled anode at SU, a hydrogen/air front is formed that temporarily divides the cell into two regions of different character, a H_2/air fuel cell in the inlet region and an electrolyzer in the outlet region. As shown in **Fig. 5**, the SU process gives rise to a potential transient duration of approximately 2s, which roughly corresponds to the time estimated for the H_2-air front to reach the anode outlet. The interaction of both regions drives the cathode potential near the anode outlet region (RE9 in our cell set up) to elevated values, favoring corrosion of the electrode in this region.

A similar phenomenon occurs during SD, when the anode is purged with air to remove the remaining hydrogen quickly for safety reasons[31], but in this case the zone with elevated cathode potential is close to the anode inlet (RE1 in our set-up). This widely accepted mechanism has been modelled and experimentally verified by several research groups.[10-11,13,32] During SU, the cathode potential in the outlet regions (RE7, 8, 9) reaches high values, up to 1.4 V, sufficient for oxidation of the carbon catalyst support and Pt dissolution. On the other hand, the high local cathode potentials during SD (**Fig. 5.b**) are shorter in duration and localized in the region close to RE3, which corresponds to the cathode gas channel inlet zone (**Fig. 1**). Degradation of the cathode in this region, RE3, is expected to be more severe during the SD event.

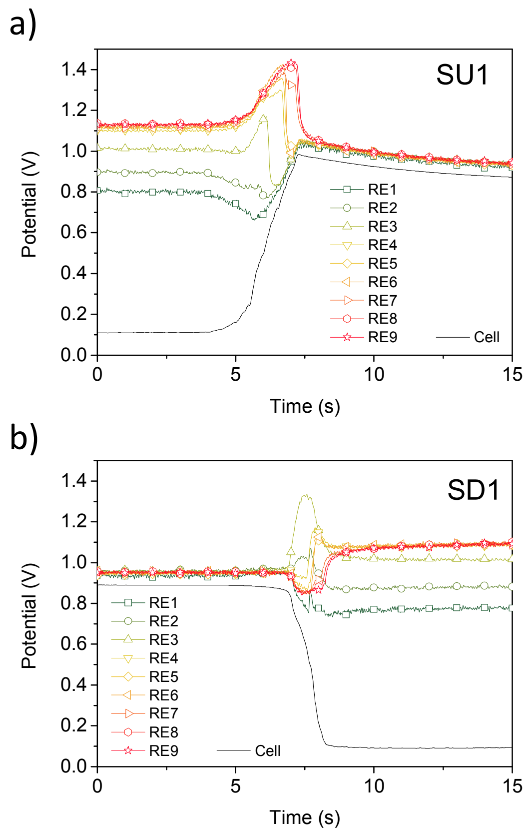

Figure 5. Transient local cathode potential response obtained under open circuit for MEA GDE30 during the first SU (a) and SD (b) cycle. Cell voltage is also included in plots. SU/SD protocol: 1) anode fed with air at open circuit (12 sl·h^{-1}, 60 s); 2) anode fed with H_2 at open circuit, (12 sl·h^{-1}, 60 s); 3) load of 0.2 A cm^{-2} (10 s ramp, 40 s hold); 4) anode fed with H_2 at open circuit (12 sl·h^{-1}, 60 s); 5) anode fed with air at open circuit, (12 sl·h^{-1}, 60 s). During cycling, cathode was fed with air at 30 sl·h^{-1}, with the cell at 80 ^{o}C and atmospheric pressure. (a) SU transition between 1 and 2; (b) SD transition between 4 and 5.

Selected local potential transients at RE1 (anode inlet), RE3 (air inlet) and RE9 (hydrogen outlet), for SU and SD are compared in **Fig. 6** for cycles 1 and 300 in all four cells. During the initial start-up events (SU1 in **Fig. 6** A), the most significant variations in local cathode potential opposite the anode outlet are obtained for GDE30, reaching values above 1.4 V. This behavior is in accordance with corrosion models that predict the most severe degradation near the outlet region during SU.[33] Among MEAs with electrosprayed cathodes, ES40 shows the highest local transient potential, followed by ES60 and ES20. After 300 cycles, potential transients at RE9 in MEAs ES60 and ES20 show the greatest change compared to the first cycle (SU1), while the ES40 and GDE30 transients are practically unchanged for SU after 300 cycles. The SU potential transients close to the anode inlet (RE1 and RE3) undergo much less significant evolution over the degradation test.

During the shut-down process, the main spike in local cathode potential is obtained at RE3 in all cases, in accordance with the models that predict major degradation near the gas inlet region during SD. As observed for SU, GDE30 has the highest transient potential value in the first cycle (SD1), increasing to above 1.3 V. No significant variation is observed in this transient after 300 SU/SD cycles. For the SD transient, noticeable changes after 300 SU/SD cycles are observed for MEAs with electrosprayed cathodes, ES60, ES40 and ES20. In particular, MEA ES20 shows a large variation in local cathode potential opposite the anode channel gas inlet (RE1) with an additional peak suggesting a change in gas transport mechanism (**Fig. 6**).

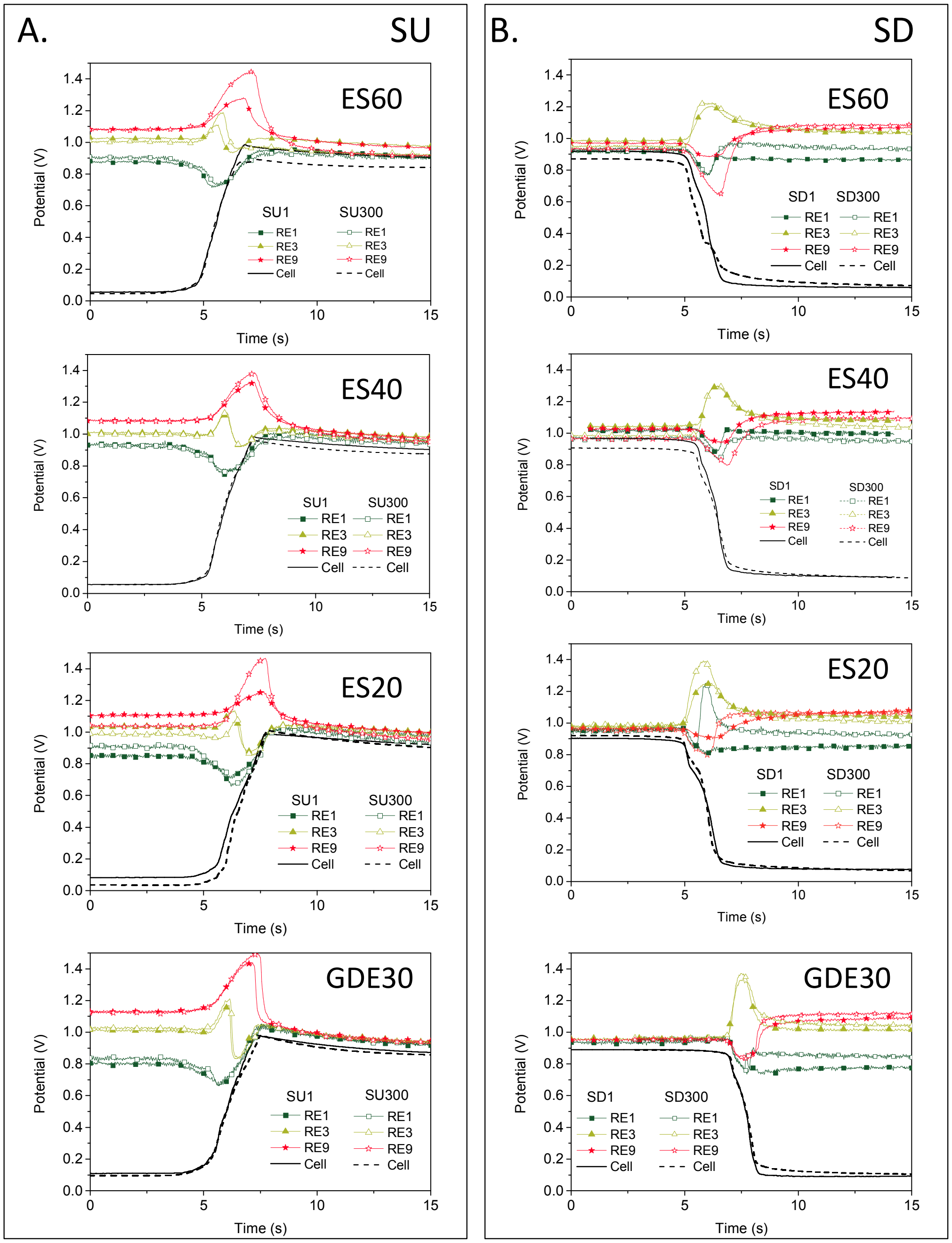

Figure 6. Comparison of local cathode potential transients under open circuit conditions at BoL and EoL (after 300 SU/SD cycles) during SU (A) and SD (B) for the four different MEAs. Only the potential measurements obtained for reference electrodes RE1, RE3 and RE9 and plotted together with cell voltage transients.

Degradation of the cell was followed during SU/SD cycling by monitoring the cell voltage under 0.2 A·cm^{-2} load. **Fig. 7** shows the evolution of cell voltage (**Fig. 7.a**) and the cell voltage decay rate (Fig. 7b) as a function of cycle number (N). The initial voltage decay rate and the decay rate measured after N=300 cycles are plotted in **Fig. 7.c** as a function of Pt:C ratio in the cathode CL. It must be noted that for the first 100 cycles, degradation rates for the cells containing ECLs are lower than that of the control cell with a commercial GDE in the cathode, reflecting a clear beneficial stabilizing effect of the ECL. The larger transient voltage observed for GDE30 MEA in Fig. 5 at BoL could be related to this different behavior. After this period, the decay rate stabilizes at a value that maintains a direct proportionality with the Pt:C ratio in the cathode CL. This behavior suggests that after an activation period probably due to porosity loss, the degradation is linked to the Pt:C ratio in the cathode CL (or the Pt volumetric concentration in the cathode CL). This is consistent with reports showing that the electro-oxidation of carbon electrodes is catalyzed by the presence of Pt.[34]

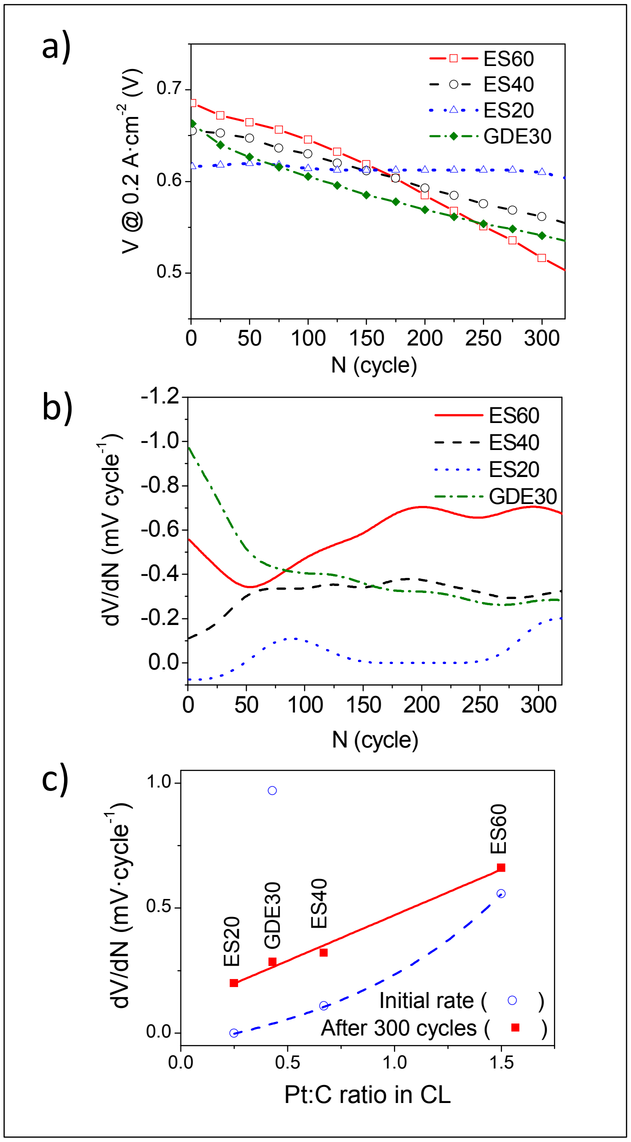

Figure 7. a) Cell voltage decay, measured at 0.2 A·cm^{-2}, as a function of SU/SD cycle number. Inset: expansion of initial cycles. b) Decay rate from plot (a). c) Initial voltage decay rate and voltage decay rate after 300 cycles as a function of Pt:C ratio in the cathode CL.

The lower initial degradation rates with electrosprayed layers shown in **Fig. 7c** may be related to the specific properties of the cathode CL. According to a previous work[16], electrosprayed layers present a highly hydrophobic character that improves water removal from the cell, leading to more homogeneous cell response. A second consequence of the high hydrophobicity of the ECL is a certain loss in catalytic activity of Pt for oxygen reduction within the ECL, as shown by impedance results in the same work. This lower water content might also effectively retard the carbon corrosion and Pt dissolution processes. Carbon corrosion accelerates under high humidification conditions[35-36], basically because water participates in the reaction (reaction (4)), and increased humidification favors a decrease in the carbon oxidation overpotential [37]. Dissolution of Pt and subsequent diffusion through the ionomer phase increases with the level of humidification in the cell and accelerates degradation via reactions (2) and (3).[38-39]

$$Pt + H_2O \rightarrow PtO + 2H^+ + 2e^- \qquad (2)$$

$$Pt \rightarrow Pt^{2+} + 2e^- \qquad (3)$$

$$C + 2H_2O \rightarrow CO_2 + 4H^+ + 4e^- \qquad (4)$$

Beyond 100 SU/SD cycles, the degradation rates follow the Pt:C ratios in the cathode CLs, as shown in **Figs. 7b** and **7c**. After this point the effects of previous cycles on the morphology, porosity and/or hydrophobicity of the electrosprayed layers have negated their benefits for cell stability, leading to a degradation fully dependent on Pt catalyst concentration within the CL. A similar dependence of the degree of degradation on Pt:C ratio has been found by Speder et al. using a different SU/SD cycling protocol[40], which must be attributed to the catalytic effect of Pt on carbon corrosion.[41]

Post degradation performance

The impact of the SU/SD cycling protocol on cell performance can be assessed in **Figs. 4.C and 4.D** in comparison with the BoL polarization curves in **Figs. 4.A and 4.B**. Changes in the global polarization curves are reflected in the values of parameters of these curves (Table 2). The most relevant are the decrease in i_0 and increase of $R_i(dc)$. The i_0 decrease is a consequence of the reduction in ECSA, which is significant for ES60, ES40 and GDE30 (> 70%), compared with ES20 (< 10%). Larger $R_i(dc)$ values, on the other hand, reflect slower electronic, protonic and mass transport processes. This increase follows the same trend as the decreasing i_0, i.e. almost a factor of 4 for ES60, compared with 3.3, 1.4, and 2.4, for ES40, ES20, and GDE30, respectively. The degree of degradation after 300 SU/SD cycles follows the Pt:C ratio in the MEA: ES60 > ES40 > GDE30 > ES20, in agreement with the trends observed in degradation rates in Fig. 7c.

More severe degradation observed for ES60 and ES40 is accompanied by greater dispersion from inlet to outlet of the local cathode potentials after 300 SU/SD cycles (Fig. 4.C). In these two MEAs, the localized polarization curves show a clear differentiation of the cell area into two regions: the first opposite the anode inlet (RE1-RE2-RE3) and the second opposite the anode outlet (from RE4 to RE9). In contrast, for the ES20 cathode the global polarization curve and dispersion of local cathode potentials are less affected by SU/SD cycling.

By analyzing the local cathode potentials individually, the internal resistance values were calculated using Equation 1. **Fig. 8** compares those values at BoL (**Fig. 8.A**) and after 300 SU/SD cycles (**Fig. 8.B**) for the four cells. The plots all indicate the same trend; there is an increase in internal resistance in the region from RE4 to RE9, the magnitude of which is mainly dependent on the Pt:C ratio in the cathode CL. The ES20 MEA, with the lowest Pt:C ratio, shows the highest stability against degradation by SU/SD events.

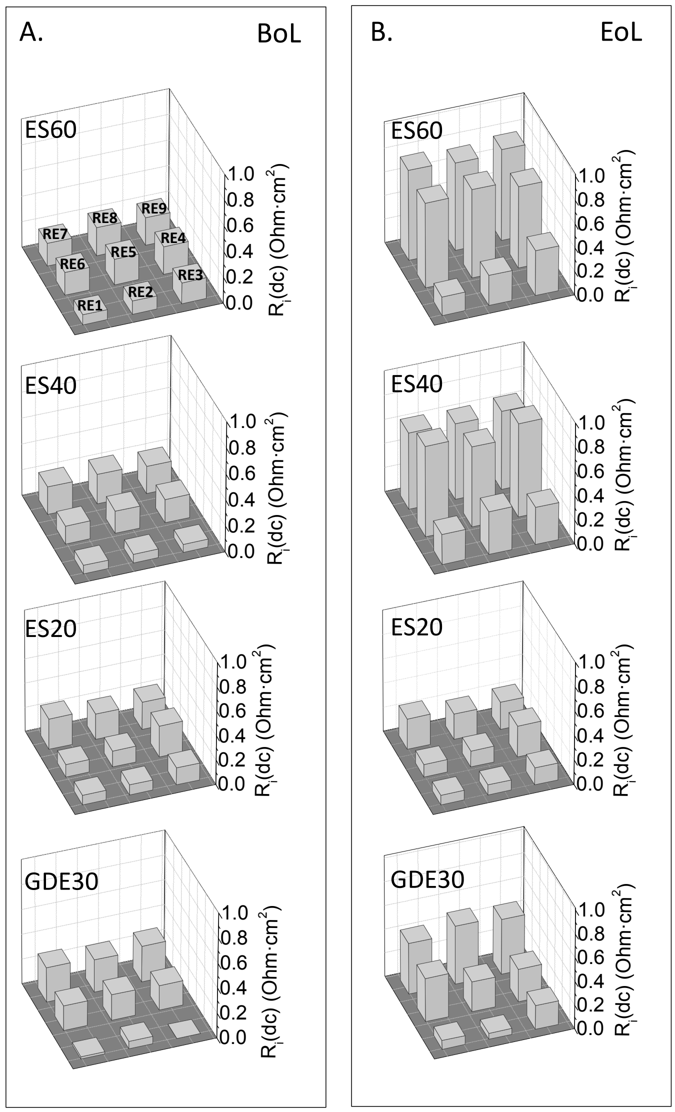

Figure 8. Distribution of localized polarization resistance values in the four different cells at BoL (A) and EoL (B).

According to the results obtained from localized measurements, the degradation effects were particularly severe in the region near the gas outlet in all MEAs studied. Similar findings have been reported by Ishigami et al.[42-43]

In order to address the origin of the observed differences, a post-mortem characterization of the MEAs was performed by SEM by analyzing the region close to the gas outlet, where the increase in internal resistance was most significant. **Fig. 9** compiles the micrographs taken from cathode CL cross-sections in the region close to RE7 for all MEAs tested. These images are presented in comparison with those of the original cathode CLs after compression between the flow-field plates. The BoL images (Fig. 9A) show that the porosity of the ECLs is not substantially modified by compression.

The drastic volume reduction observed for ES60 and ES40 at EoL is evident from comparison of Figs. 8A and 8B. In particular for ES60, the precipitated Pt band inside the Nafion membrane can be easily distinguished, whereas Pt remaining at the electrode is highly sintered in that zone. The Pt precipitation inside the polymer membrane seems to occur to some extent in all the MEAs tested. The mass reduction by corrosion in the GDE30 CL, and even in the MPL it was deposited on, is also noticeable from the higher void volume inside the MEA compared with the pristine sample. Similar evidence has been reported by Ishigami et al. from analysis of samples from the inlet, middle and outlet of an MEA degraded by start-stop cycles.[42] Mass loss by corrosion is probably the origin of the breakdown in adherence between the CL, MPL and membrane. The ES20 CL has lost part of its volume, although its porous structure is relatively well preserved, in contrast with the rest of the samples. Taking into account that all cathode CLs contain the same Pt loading (0.25 $mg\cdot cm^{-2}$), the CL prepared with a low Pt:C ratio by electrospraying, with a highly porous microstructure, provides high resistance against degradation by start-stop cycling.

The specific reason for this improved resistance is difficult to determine. The major differences between ECLs and conventionally deposited layers are their different ionomer distribution and higher porosity. These two characteristics contribute to the high hydrophobicity of these layers, but it is difficult to state conclusively which of these properties, or a combination of them, is the origin of the observed behavior.

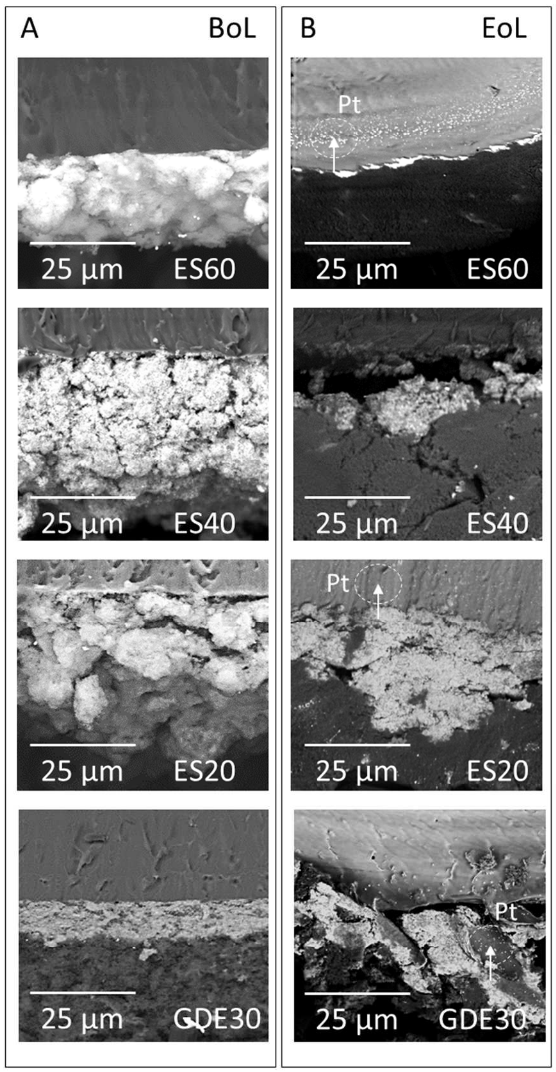

Figure 9. SEM micrograph of the cross-sections of the cathode catalyst layers. A) Pristine CLs after MEA compression at BoL. B) CLs at the RE7 region of the MEA at EoL.

It must be emphasized that the evident degradation observed for all the MEAs at the cathode CL near RE7 is not homogeneous throughout the whole active area. Further analysis of these samples at the inlet zone (near RE3) reveals a lower degree of degradation at the CL cathodes. A detailed localized physico-chemical post-mortem study regarding the effects of SU/SD cycling, not only at the cathode CL, but at the MPL and the GDL substrate at the cathode and the anode, is in progress.

In summary, the results indicate that degradation by SU/SD cycling on cells with electrosprayed cathodes follows a different behavior compared to a standard electrode. The application of a deposition technique such as electrospraying to produce highly porous catalyst layers may be an adequate mitigation strategy to reduce degradation. Electrosprayed morphology has two important benefits in this respect. Firstly, it improves the homogeneity of cell response, which mitigates deleterious effects caused by local water accumulation in the cell.[12,44-45] In addition, the porous morphology provides high hydrophobic character to the CL, which probably works under lower water contents than conventional layers. Under these conditions, corrosion kinetics is less favored leading to more durable layers. The beneficial effects of electrosprayed layers have a limited durability, probably as a consequence of the progressive loss of porosity, compaction of the layers, and increased hydrophilicity with SU/SD cycling. As a consequence, after a certain number of cycles, the measured degradation rate depends on other factors, such as the Pt:C ratio in the cathode.

CONCLUSIONS

Cathode catalyst layers prepared by an electrospray technique have been studied for durability under repeated start-up/shut-down conditions.

An innovative array of local reference electrodes was used to investigate the SU/SD mechanism and measure local performance degradation.

Most severe cathode degradation occurred in areas opposite the anode outlet, which experienced the highest transient potentials during start-up.

Degradation was characterized by an initial period of rapid decay in performance followed by a more gradual decay to a steady state value.

Electrosprayed cathode CLs showed a slower decay rate during the initial period (100 cycles), showing that the microstructure of the cathode CL plays an important role in the rate of this degradation process.

The long-term degradation rate increased with Pt:C ratio in the CL due to the catalytic effect of Pt on carbon corrosion.

AUTHOR INFORMATION

Corresponding Author

* Paloma Ferreira-Aparicio. CIEMAT-Centro de Investigaciones Energéticas, Medioambientales y Tecnológicas. Avda. Complutense 40, E-28040. Madrid. Spain. paloma.ferreira@ciemat.es. Tel: +34 91 3460897. Fax: +34 91 3466269.

Author Contributions

The manuscript was written through contributions of all authors. All authors have given approval to the final version of the manuscript. ‡These authors contributed equally.

Funding Sources

P. Ferreira-Aparicio, A.M. Chaparro, M.A. Folgado and J. J. Conde received funding from the National Programme for Fostering Excellence in Scientific and Technical Research (2015 call) under contract E-LIG-E (ENE2015 70417-P).

E. Brightman and G. Hinds received funding from EU FP7 H2FC project (Grant Agreement Number 284522) under user access project number 2039.

ABBREVIATIONS

BP bipolar plate; CL catalyst layer; ECL electrosprayed catalyst layer; ECSA electrochemical surface area; GDE gas diffusion electrode; GDL gas diffusion layer; HSAAC high surface area advanced carbon; MEA membrane-electrode assembly; MPL microporous layer; PEMFC proton exchange membrane fuel cell; RE reference electrode; RHE reversible hydrogen electrode; SU startup; SD shutdown.

REFERENCES

(1) Fuel Cell Technologies Office Multi-Year Research, Development, and Demonstration Plan (updated September 2016). https://energy.gov/eere/fuelcells/downloads/fuel-cell-technologies-office-multi-year-research-development-and-22 (last accessed Feb. 2017).

(2) Borup, R.; Mukundan, R.; Spernjak, D.; Baker, A.; Lujan, R.; Langlois, D.; Ahluwalia, R.; Papadias, D. D.; Weber, A.; Kusoglu, A.; Shi, S.; More, K.; Grot, S. Durability Improvements

through Degradation Mechanism Studies. DOE Hydrogen and Fuel Cells Program. *FY 2015 Annual Progress Report.* 2016. V–101.

(3) Wu, J.; Yuan, X.Z.; Martin, J.J.; Wang, H.; Zhang, J.; Shen, J.; Wu, S.; Merida, W. A Review of PEM Fuel Cell Durability: Degradation Mechanisms and Mitigation Strategies. *J. Power Sources* **2008**, *184*, 104-119.

(4) Yousfi-Steiner, N.; Mocotéguy, Ph.; Candusso, D.; Hissel, D. A Review on Polymer Electrolyte Membrane Fuel Cell Catalyst Degradation and Starvation Issues: Causes, Consequences and Diagnostic for Mitigation. *J. Power Sources* **2009**, *194*, 130-45.

(5) Schulze, M.; Knöri, T.; Schneider, A.; Gülzow, E.. Degradation of Sealings for PEFC Test Cells during Fuel Cell Operation. *J. Power Sources* **2004**, *127*, 222-229.

(6) de Bruijn, F. A.; Dam, V. A. T.; Janssen, G. J. M. Review: Durability and Degradation Issues of PEM Fuel Cell Components, *Fuel Cells* **2008**, *8*, 3-22.

(7) Ji, M.; Wei, Z. A Review of Water Management in Polymer Electrolyte Membrane Fuel Cells. *Energies* **2009**, 1057-1060.

(8) Jiao, K.; Li, X. Water Transport in Polymer Electrolyte Membrane Fuel Cells: Review. *Prog. Energy Combust Sci.* **2011**, *37,* 221-291.

(9) Li, H.; Tang, Y.; Wang, Z.; Shi, Z.; Wu, S.; Song, D.; Zhang, J.; Fatih, K.; Zhang, J.; Wang, H.; Liu, Z.; Abouatallah, R.; Mazza, A. A Review of Water Flooding Issues in the Proton Exchange Membrane Fuel Cell. *J. Power Sources* **2008**, *178*, 103-117.

(10) Maranzana, G.; Lamibrac, A.; Dillet, J.; Abbou, S.; Didierjean, S.; Lottin, O. Startup (and Shutdown) Model for Polymer Electrolyte Membrane Fuel Cells. *J. Electrochem. Soc.* **2015**, *162*, F694-F706.

(11) Chen, J.; Hu, J.; Waldecker, J. R., A Comprehensive Model for Carbon Corrosion during Fuel Cell Start-Up. *J. Electrochem. Soc.* **2015**, *162*, F878-F889.

(12) Reiser, C.A.; Bregoli, L.; Patterson, T.W.; Yi, J.S.; Yang, J.D.; Perry, M.L.; Jarvi, T.D. A Reverse-Current Decay Mechanism for Fuel Cells. *Electrochem. Solid-State Lett.* **2005**, *8* , A273-A276.

(13) Dillet, J.; Spernjak, D.; Lamibrac, A.; Maranzana, G.; Mukundan, R.; Fairweather, J.; Didierjean, S.; Borup, R.L.; Lottin, O. Impact of Flow Rates and Electrode Specifications on Degradations during Repeated Startups and Shutdowns in Polymer-Electrolyte Membrane Fuel Cells. *J. Power Sources* **2014**, *250*, 68-79.

(14) Kreitmeier, S.; Wokaun, A.; Büchi, F. N. Local Catalyst Support Degradation During Polymer Electrolyte Fuel Cell Start-Up and Shutdown. *J. Electrochem. Soc.* **2012**, *159*, F787-F793.

(15) Weber, A. Z.; Borup, R. L.; Darling, R. M.; Das, P. K.; Dursch, T. J.; Gu, W.; Harvey, D.; Kusoglu, A.; Litster, S.; Mench, M. M.; Mukundan, R.; Owejan, J. P.; Pharoah, J. G.; Secanell, M.; Zenyuka, I. V. A Critical Review of Modeling Transport Phenomena in Polymer-Electrolyte Fuel Cells. *J. Electrochem. Soc.* **2014**, *161*, F1254-F1299.

(16) Chaparro, A.M.; Ferreira-Aparicio, P.; Folgado, M.A.; Brightman, E.; Hinds, G. Study of Superhydrophobic Electrosprayed Catalyst Layers Using a Localized Reference Electrode Technique. *J. Power Sources* **2016**, *325*, 609-619.

(17) Hinds, G.; Brightman, E. In Situ Mapping of Electrode Potential in a PEM Fuel Cell. *Electrochem. Commun.* **2012**, *17*, 26-29.

(18) Chaparro, A. M.; Folgado, M. A.; Ferreira-Aparicio, P.; Martín, A. J.; Alonso-Álvarez, I.; Daza, L. Properties of Catalyst Layers for PEMFC Electrodes Prepared by Electrospray Deposition. *J. Electrochem. Soc.* **2010**, *157*, B993-B999.

(19) Chaparro, A.M.; Ferreira-Aparicio, P.; Folgado, M.A.; Martín, A.J.; Daza, L. Catalyst Layers for Proton Exchange Membrane Fuel Cells Prepared by Electrospray Deposition on Nafion Membrane. *J. Power Sources* **2011**, *196*, 4200–4208.

(20) http://www.jmj.co.jp/fuel/img/hispec_catalysts_internal_oct_06_1.pdf , (last accessed on Nov. 2016)

(21) Ferreira-Aparicio, P. New Insights into Proton Surface Mobility Processes in PEMFC Catalysts Using Isotopic Exchange Methods. *ACS Appl. Mater. Interfaces* **2009**, *1*, 1946-1957.

(22) Chaparro, A.M.; Gallardo, B.; Folgado, M.A.; Martín, A.J.; Daza, L. PEMFC Electrode Preparation by Electrospray: Optimization of Catalyst Load and Ionomer Content. *Catal. Today* **2009**, *143*, 237-241.

(23) Folgado, M.A; Ferreira-Aparicio, P; Chaparro, A. M. An Optical and Single Cell Study of the Assembly of a PEMFC with Dry and Expanded Nafion. *Int. J. Hydrogen Energy* **2016**, *41*, 505-515.

(24) Ferreira-Aparicio, P. PEMFC Catalysts Synthesis and Characterization: Relevance of Structural and Chemical Factors on Surface Diffusion Processes. *Electrochem. Solid State Lett.* **2009**, *12*, B38-B42.

(25) Brightman, E.; Hinds, G. In Situ Mapping of Potential Transients During Start-Up and Shut-Down of a Polymer Electrolyte Membrane Fuel Cell. *J. Power Sources* **2014**, *267*, 160-170.

(26) Ferreira-Aparicio, P.; Gallardo-López, B.; Chaparro, A.M.; Daza, L. Physico-Chemical Study of the Degradation of Membrane-Electrode Assemblies in a Proton Exchange Membrane Fuel Cell Stack. *J. Power Sources* **2011**, *196*, 4242–4250.

(27) Chaparro, A.M.; Martín, A.J.; Folgado, M.A.; Gallardo, B.; Daza, L. Comparative Analysis of the Electroactive Area of Pt/C PEMFC Electrodes in Liquid and Solid Polymer Contact by Underpotential Hydrogen Adsorption/Desorption. *Int. J. Hydrogen Energy* **2009**, *34,* 4838-4846.

(28) Saha, M.S.; Malevich, D.; Halliop, E.; Pharoah, J. G.; Peppley, B. A.; Karan, K. Electrochemical Activity and Catalyst Utilization of Low Pt and Thickness Controlled Membrane Electrode Assemblies. *J. Electrochem. Soc.* **2001**, *158*, B562-B567.

(29) Shukla, S.; Stanier, D.; Saha, M. S.; Stumper, J.; Secanell, M. Analysis of Inkjet Printed PEFC Electrodes with Varying Platinum Loading. *J. Electrochem. Soc.* **2016**, *163*, F677-F687.

(30) Eikerling, M. Water Management in Cathode Catalyst Layers of PEM Fuel Cells. a Structure-Based Model. *J. Electrochem. Soc.2006*, *153*, E58-E70.

(31) Hartnig, C.; Schmidt, T. J. Simulated Start–Stop as a Rapid Aging Tool for Polymer Electrolyte Fuel Cell Electrodes. *J. Power Sources* **2011**, *196*, 5564-5572.

(32) Tang, H.; Qi, Z.; Ramani, M.; Elter, J. F. PEM Fuel Cell Cathode Carbon Corrosion Due to the Formation of Air/Fuel Boundary at the Anode. *J. Power Sources* **2006**, *158*, 1306-1312.

(33) Lamibrac, A.; Maranzana, G.; Lottin, O.; Dillet, J.; Mainka, J.; Didierjean, S.; Thomas, A.; Moyne, C. Experimental Characterization of Internal Currents During the Start-up of a Proton Exchange Membrane Fuel Cell. *J. Power Sources* **2011**, *196*, 9451-9458.

(34) Willsau, J.; Heitbaum, J. The Influence of Pt-Activation on the Corrosion of Carbon in gas Diffusion Electrodes-A Dems Study. *J. Electroanal. Chem.* **1984**, *161*, 93-101.

(35) Hu, J.; Su, P.C.; Kumar, S.; Djilali, N. Modelling and Simulations of Carbon Corrosion During Operation of a Polymer Electrolyte Membrane Fuel Cell. *Electrochim. Acta* **2009**, *54*, 5583-5592.

(36) Hashimasa, Y;. Matsuda, Y.; Shimizu, T. Comparison of Carbon Corrosion Test Methods for Polymer Electrolyte Fuel Cell. *Electrochim. Acta* **2015**, *179*, 119-125.

(37) Takeuchi, N.; Fuller, T. Modeling and Investigation of Carbon Loss on the Cathode Electrode During PEMFC Operation. *J. Electrochem. Soc.* **2010**, *157*, B135-B140.

(38) Bi, W.; Sun , Q.; Deng, Y.; Fuller, T. The Effect of Humidity and Oxygen Partial Pressure on Degradation of Pt/C Catalyst in PEM Fuel Cell. *Electrochim. Acta* **2009**, *54,* 1826-1833.

(39) Li, Y.; Moriyama, K.; Gu, W.; Arisetty, S.; Wang, C. Y. A One-Dimensional Pt Degradation Model for Polymer Electrolyte Fuel Cells. *J. Electrochem. Soc.* **2015**, *162*, F834-F842.

(40) Speder, J.; Zana, A.; Spanos, I.; Kirkensgaard, J.; Mortensen, K.; Hanzlik, M.; Arenz, M. Comparative Degradation Study of Carbon Supported Proton Exchange Membrane Fuel Cell Electrocatalysts: the Influence of the Platinum to Carbon Ratio on the Degradation Rate. *J. Power Sources* **2014**, *261*, 14-22.

(41) Park, Y.-C.; Kakinuma, K.; Uchida, M.; Tryk, D.A.; Kamino, T.; Uchida, H.; Watanabe, M. Investigation of the Corrosion of Carbon Supports in Polymer Electrolyte Fuel Cells Using Simulated Start-Up/Shutdown Cycling. *Electrochim. Acta* **2013**, *91*, 195-207.

(42) Ishigami, Y. ; Takada, K; Yano, H; Inukai, J., Uchida, M.; Nagumo, Y; Hyakutake, T.; Nishide, H.; Watanabe, M. Corrosion of Carbon Supports at Cathode During Hydrogen/Air Replacement at Anode Studied by Visualization of Oxygen Partial Pressures in a PEFC—Start-Up/Shut-Down Simulation. *J. Power Sources* **2011**, *196*, 3003-3008.

(43) Ishigami,Y.; Maeda, I.; Takada, K.; Hyakutake, T.; Suga,T.; Inukai, J.; Uchida,M.; Nagumo, Y.; Nishide,H.; Watanabe, M. Real-Time Visualization of CO2 Generated by Corrosion of the Carbon Support in a PEFC Cathode. *Electrochem. Solid-State Lett.* **2012**, *15*, B51-B53.

(44) Ohyagia, S.; Matsuda, T.; Iseki, Y.; Sasaki, T.; Kaito, C. Effects of Operating Conditions on Durability of Polymer Electrolyte Membrane Fuel Cell Pt Cathode Catalyst Layer. *J. Power Sources* **2011**, *196*, 3743-3749.

(45) Patterson, T.W.; Darling, R.M. Damage to the Cathode Catalyst of a PEM Fuel Cell Caused by Localized Fuel Starvation. *Electrochem. Solid State Lett.* **2006**, *9*, A183-A185.

Table of Contents Graphic

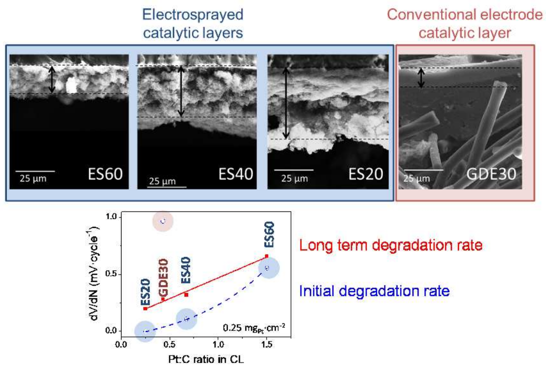

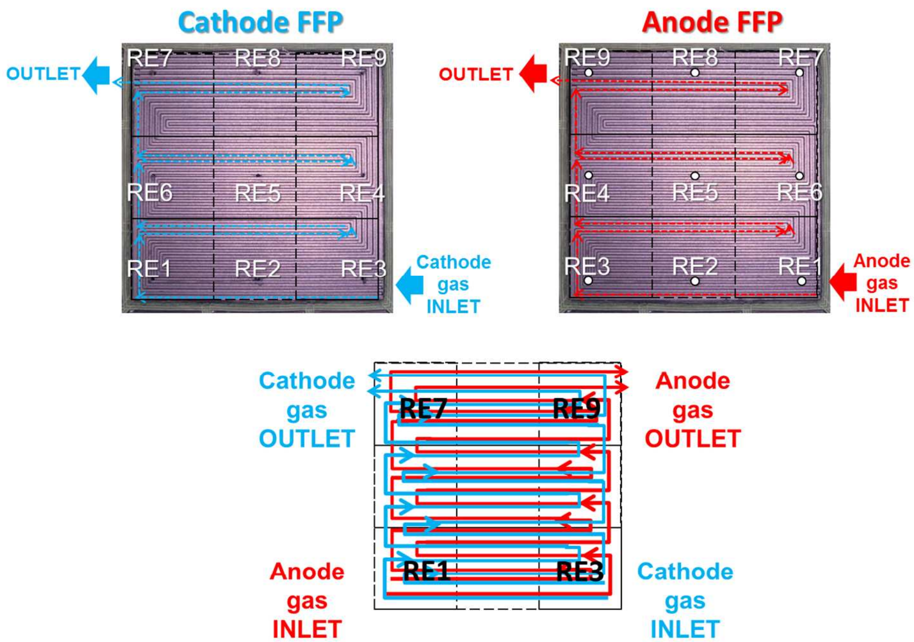

Figure 1. Location of the array of localized reference electrodes at the cathode with respect to the channels of the flow field plates (FFPs) of anode and cathode.

Fig. 1

262x183mm (150 x 150 DPI)

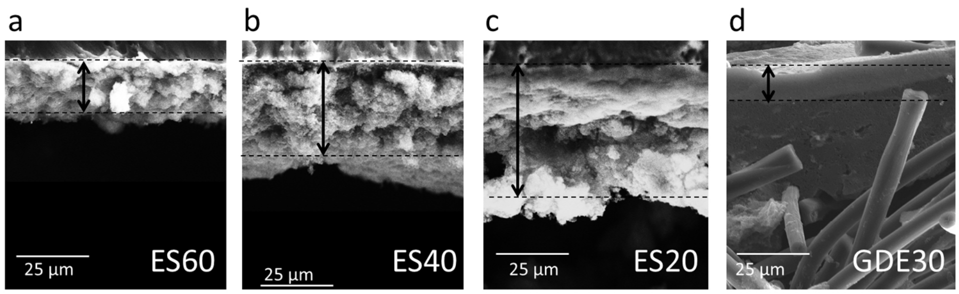

Figure 2. SEM micrographs of the cross-sections of pristine cathode electrodes: a) catalyst layer of the electrosprayed Pt(60wt%) on HSAAC on NRE212 (MEA ES60); b) catalyst layer of the electrosprayed Pt(40wt%) on Vulcan XC72 on NRE212 (MEA ES40); c) catalyst layer of the electrosprayed Pt(20wt%) on Vulcan XC72 on NRE212 (MEA ES20); d) standard gas diffusion electrode (ELAT-GDE- LT250EWALTSI) with Pt(30wt%) on Vulcan XC72 anode in ES60, ES40, ES20, and anode and cathode in GDE30.
Fig. 2
288x98mm (150 x 150 DPI)

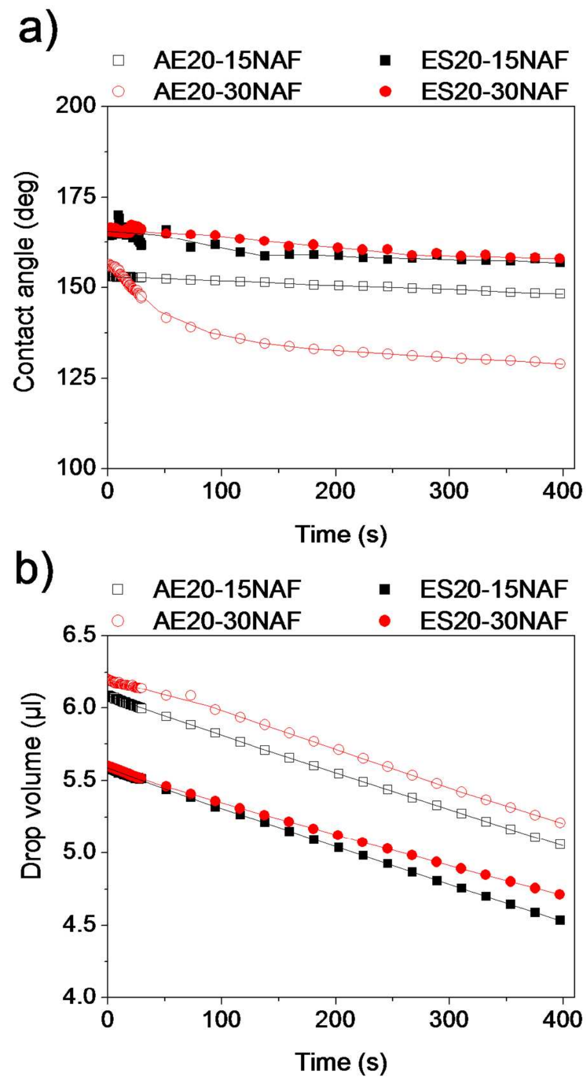

Figure 3. a) Water contact angles measured as a function of time on the surface of catalyst layers prepared by electrospray and aerography with 15 and 30 wt% ionomer. b) Evolution of the water drop volume with time. Symbols: aerography (open symbols); electrospray (solid symbols); 15wt% Nafion ionomer (squares), 30wt% Nafion ionomer (circles).

Fig. 3

220x372mm (150 x 150 DPI)

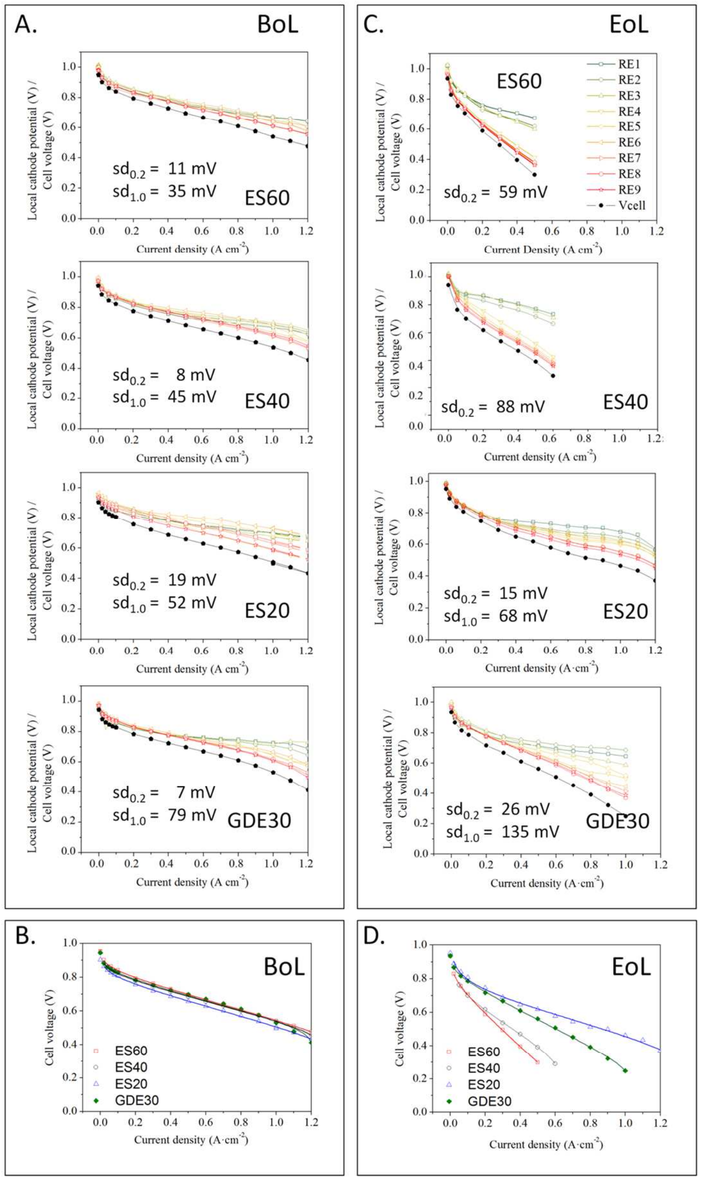

Figure 4. A) Cell voltage and local cathode potential as a function of current density at BoL for the four different MEAs. B) Comparison of polarization curves for the four MEAs at BoL. C) Cell voltage and local cathode potential as a function of current density at EoL (after 300 SU/SD cycles). D) Comparison of polarization curves for the four MEAs at EoL. Standard deviations of potential values at 0.2A·cm^{-2} ($sd_{0.2}$) and 1.0 A·cm^{-2} ($sd_{1.0}$) are indicated in A and C for each MEA.

Fig. 4

216x348mm (150 x 150 DPI)

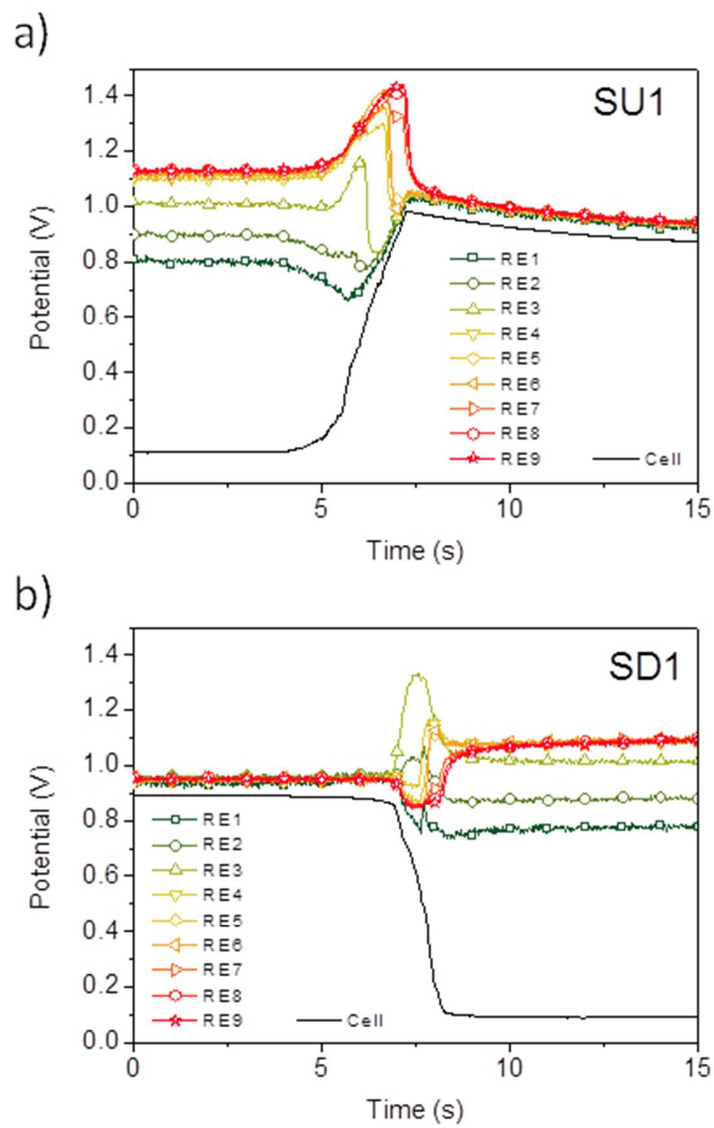

Figure 5. Transient local cathode potential response obtained under open circuit for MEA GDE30 during the first SU (a) and SD (b) cycle. Cell voltage is also included in plots. SU/SD protocol: 1) anode fed with air at open circuit (12 sl·h^{-1}, 60 s); 2) anode fed with H2 at open circuit, (12 sl·h^{-1}, 60 s); 3) load of 0.2 A cm^{-2} (10 s ramp, 40 s hold); 4) anode fed with H_2 at open circuit (12 sl·h^{-1}, 60 s); 5) anode fed with air at open circuit, (12 sl·h^{-1}, 60 s). During cycling, cathode was fed with air at 30 sl·h^{-1}, with the cell at 80 ^{o}C and atmospheric pressure. (a) SU transition between 1 and 2; (b) SD transition between 4 and 5.
Fig. 5
85x116mm (150 x 150 DPI)

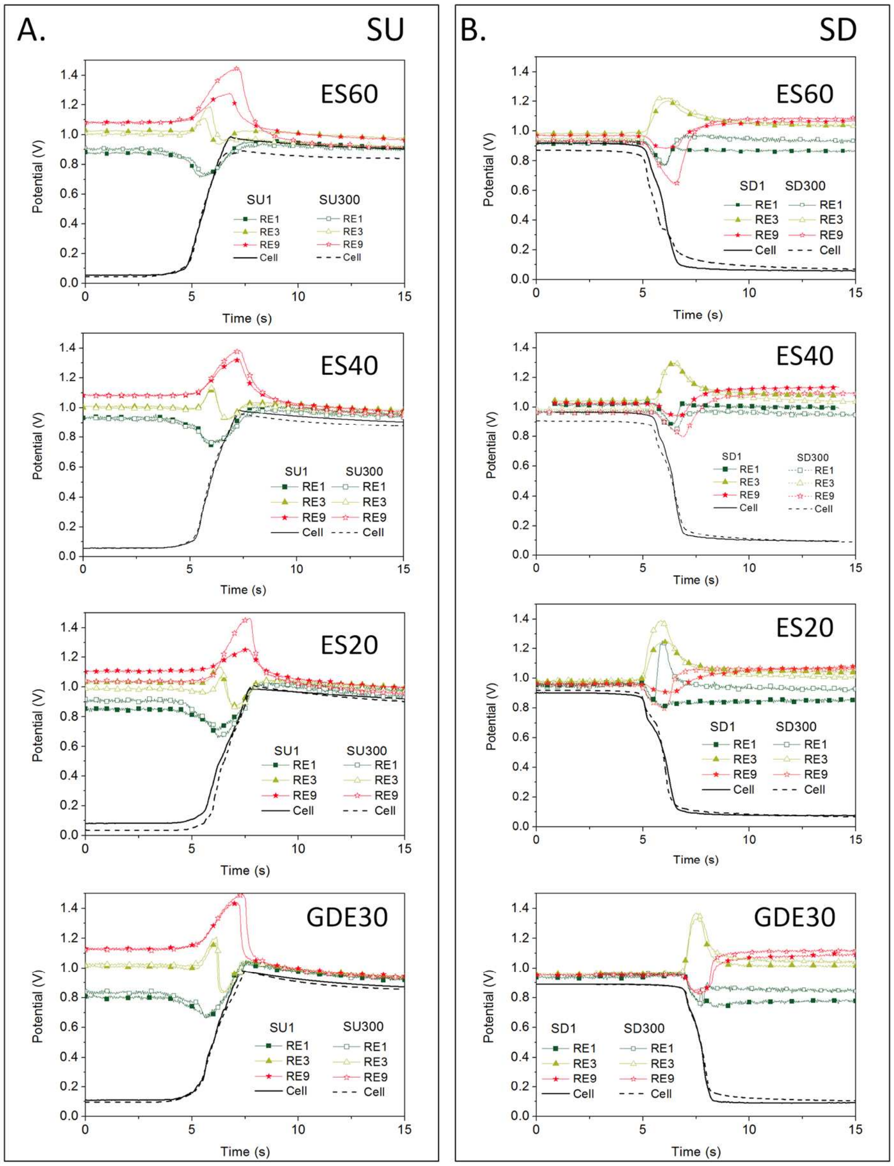

Figure 6. Comparison of local cathode potential transients under open circuit conditions at BoL and EoL (after 300 SU/SD cycles) during SU (A) and SD (B) for the four different MEAs. Only the potential measurements obtained for reference electrodes RE1, RE3 and RE9 and plotted together with cell voltage transients.
Fig. 6
316x406mm (150 x 150 DPI)

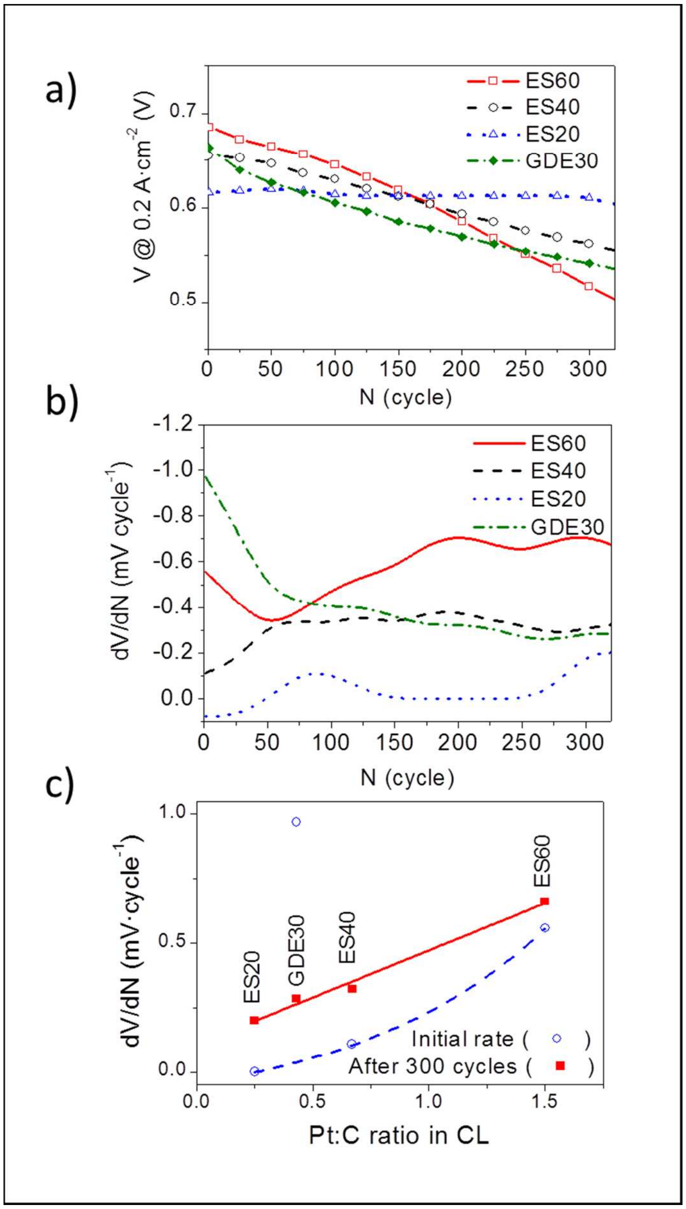

Figure 7. a) Cell voltage decay, measured at 0.2 A·cm^{-2}, as a function of SU/SD cycle number. Inset: expansion of initial cycles. b) Decay rate from plot (a). c) Initial voltage decay rate and voltage decay rate after 300 cycles as a function of Pt:C ratio in the cathode CL

Fig. 7

131x232mm (150 x 150 DPI)

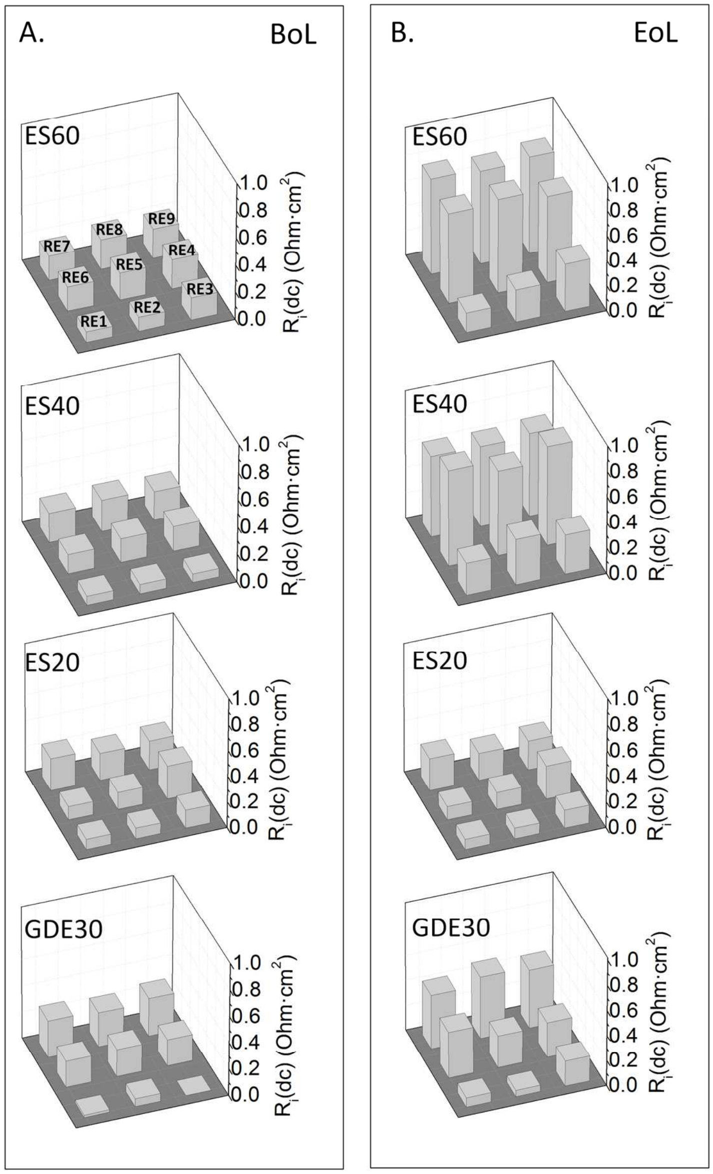

Figure 8. Distribution of localized polarization resistance values in the four different cells at BoL (A) and EoL (B).
Fig. 8
264x399mm (150 x 150 DPI)

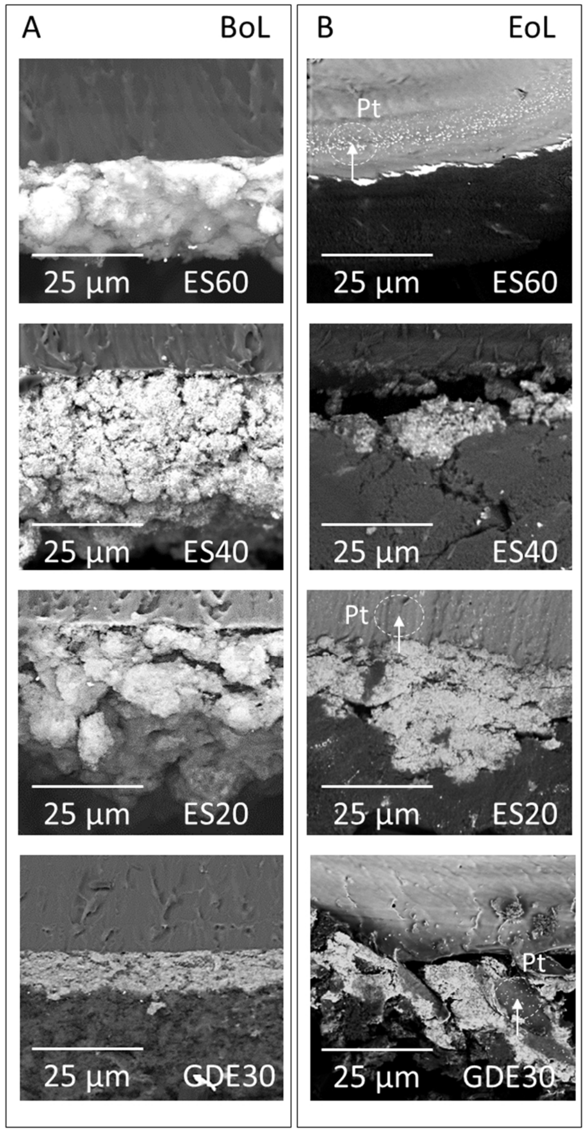

Figure 9. SEM micrograph of the cross-sections of the cathode catalyst layers. A) Pristine CLs after MEA compression at BoL. B) CLs at the RE7 region of the MEA at EoL.
Fig. 9
115x226mm (150 x 150 DPI)

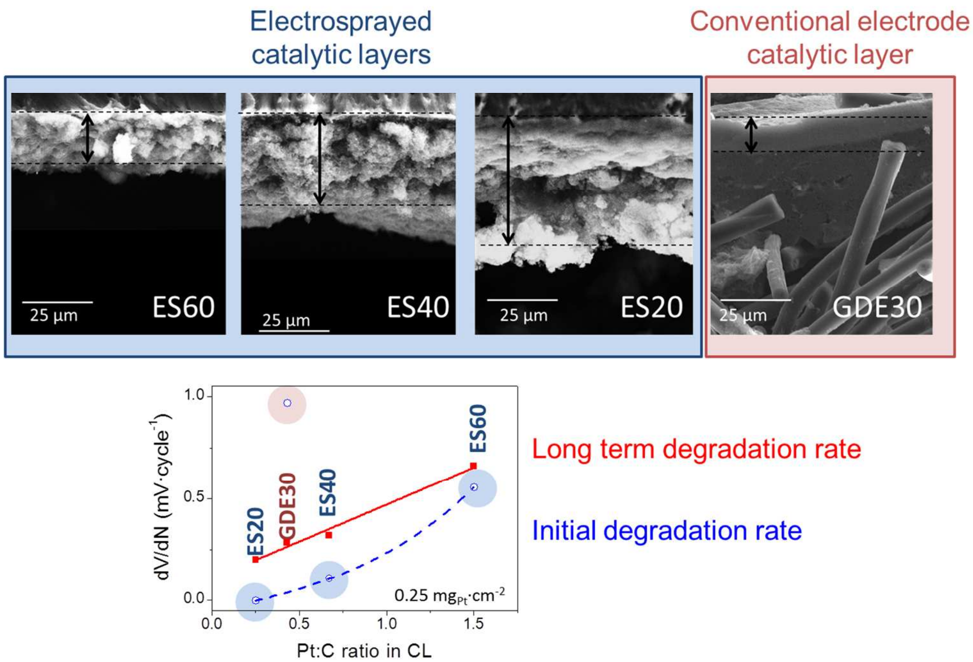

Table of Contents. The aging by startup/shutdown cycling of PEM fuel cells with electrosprayed cathode catalyst layers has been analyzed using localized measurements of cathode potential. The porous electrospray-generated microstructure slows down cells degradation notably. Initial degradation cycles lead to compaction and porosity loss in catalyst layers. Long-term degradation depends on the Pt:C ratio in the cathode catalyst layer.
Table of Contents
257x174mm (150 x 150 DPI)